Supporting Information

Saibil et al. 10.1073/pnas.1211976109

SI Materials and Methods

Yeast Strains, Constructs, and Media. Yeast strains of the 74D-694 background (1) that contained a deletion of the NM domain in the endogenous SUP35 gene (2) were grown on standard synthetic media lacking particular amino acids/bases and containing either D-glucose or D-galactose as the carbon source. They contained a fusion construct consisting of the prion domain (amino acids 1–253) of Sup35 fused to either GFP [NM-GFP (3)] or an HA, myc, or FLAG tag via an 8-aa linker (GSRVPVEK) that was stably integrated into the genome, under control of the GPD or Gal1 promoter, respectively. Dot cells with the NM construct expressed under control of the GPD promoter propagated the dots constitutively. Cells were produced for microscopy by overnight growth. Ring cells were de novo–induced for ∼24–30 h in media containing D-galactose before high-pressure freezing or fluorescence microscopy.

For colocalization studies of NM-YFP with different molecular chaperones, the genomic copies of indicated chaperones were fused with Cerulean (4) at their C termini in haploid cells according to Wach et al. (5) and confirmed by PCR. The fusions were created either in a strain that harbored NM-YFP as an inducible genomic copy to allow for the ring and ribbon formation typical for prion induction (2, 6) or in a strain that propagates NM-YFP constitutively in the prion state (2). All of the strains containing the corresponding fusions induced rings to the same extent as in the untagged strains and faithfully propagated the dots, indicative of the mature NM-YFP prion, for many generations. Binding of various chaperones to NM-YFP aggregates is fully consistent with their binding to [PSI^+] prion aggregates (7). Furthermore, Ssa1 binding to prion dots formed by NM-YFP in vivo has also been demonstrated by immunofluorescence (8).

To study the role of Ssa1 in fibril organization, an ssa2::Leu2, ssa3::Trp1, ssa4::Lys2 strain carrying the temperature sensitive allele ssa1-45 or wild-type ssa1 was used (9). The strain was cultured at 25°C or at 37 °C for 90 min to inactivate Ssa1-45-ts. The strains contained the 2μ plasmid p426 NM-YFP (ura) (3), and NM-YFP dots were produced upon overnight growth in synthetic complete (SC) media containing 2% galactose and lacking uracil.

Fluorescence Microscopy. Cells were grown in liquid culture to mid-log phase in glucose containing media, diluted to an OD_{600} of 0.3 before shifting the cells to galactose-containing media for ∼30 h to induce expression of NM-YFP controlled by the Gal1 promoter. For colocalization studies with different fluorescent proteins, cells were imaged with an Axioplan microscope with a 100× objective (Zeiss) and narrow band pass filters. Images were taken in one representative focal plane. Photoshop (Adobe) was used for colorization, linear adjustments of brightness and contrast, and creation of composite and merged images.

EM Sample Preparation and Data Collection. Cells were high-pressure–frozen in an EMPACT 2 freezer and freeze-substituted into Lowicryl HM20 (Polysciences) in a freeze-substitution device (EM-AFS; Leica Microsystems) by the protocol of Hawes et al. (10) with 0.2% or 2% uranyl acetate or with 0.2% glutaraldehyde, 0.1% uranyl acetate, and 1% water in acetone. Ultrathin sections were prepared using a Reichert UltracutE microtome (Leica Microsystems). Serial, dual-axis tomograms of 300-nm sections coated on one or both sides with 10-nm protein A–gold particles were collected on a Tecnai F30 microscope from −70° to 70°, in 1° intervals on a Gatan 4K camera and subsequently binned to 2K (2,000 pixels), at a pixel size of 0.744 nm for the dot samples and 1.5 nm for the ring samples. For immunolabeling, the freeze-substituted sections were blocked with 0.8% BSA in PBS and incubated with an affinity-purified polyclonal rabbit anti-YFP antibody, followed by protein A–gold (10 nm; EM Sciences).

For the cryotomograms, vitrified sections cut at a nominal thickness of 50 nm on a Leica Ultracut FC6 were mechanically attached to 300-mesh C-flat grids. Single-axis tilt series were collected over an angular range from −65° to +65°, with 1° or 2° angular increments in a Tecnai G2 Polara microscope (FEI) cooled to liquid nitrogen temperature and equipped with a Gatan postcolumn GIF 2002 energy filter. Data acquisition was done under low-dose conditions using the University of California, San Francisco (UCSF) tomography software (11). Images were recorded on a 2,000 × 2,000 pixel CCD camera at a defocus level of ∼9 μm. The pixel size at the specimen level varied between 0.6 and 1 nm. The total electron dose was around 70 e/$Å^2$.

Image Processing. Alignment of the room temperature tomograms was done with etomo (12) using the gold particles as fiducial markers. For cryotomograms, the projection images were aligned with respect to a common origin without fiducial markers, using cross-correlation (13). The alignment error of the series used for reconstruction and subsequent processing was less than 0.6 nm. This indicates that the sample, at least locally at the areas of the fibers, did not change significantly during the recording process, and the selected tilt series were properly aligned. The reconstructions were calculated using weighted back-projection algorithms and visualized with isosurface and volume-rendering techniques in the Amira software package (Mercury Computer Systems; www.amiravis.com).

The fibers show a periodic pattern, which indicates a partially ordered packing. The center-to-center distance between neighboring fibers showed a variance of ∼10 nm. This variation results in the fading of fibers neighboring the central one in the averages. Individual fibers were automatically selected according to the highest density positions in a projection image. The fibers were initially oriented by autocorrelation to determine the approximate direction of the fiber axis. The resulting subtomogram average was used as a template for subsequent alignment of subtomograms. We assumed that the translational alignment of the subtomograms was roughly correct and first aligned them rotationally based on the properties of the autocorrelation function. These show a pronounced elongation in the direction of the fiber, which defines the fiber axis direction. Then, all subtomograms were rotationally aligned with respect to each other, using the fiber array to determine the rotation angle about the fiber axes. We used a spherical mask with a diameter of ∼100 nm, which is sufficient to include the central fibril and the nearest neighbors. Each fibril was averaged independently of the other fibrils. Subsequently, when a periodicity along the fibril axis was revealed, the individual fibrils were segmented into pieces of ∼20-nm length to improve the resolution. After five iterations the alignment converged to a stable solution. The aligned subtomograms were classified with multivariate statistical analysis (14), focusing on the central fiber and surrounding region. This yielded final averages of the dot at 5.6-nm resolution and ring at 4.5-nm resolution (0.5 criterion of the Fourier shell correlation; Fig. S1*C*). The averaged maps have been deposited in the EMDB (accession nos. EMD-2103 and EMD-2104).

1. Chernoff YO, Lindquist SL, Ono B, Inge-Vechtomov SG, Liebman SW (1995) Role of the chaperone protein Hsp104 in propagation of the yeast prion-like factor [psi+]. *Science* 268:880–884.
2. Tyedmers J, et al. (2010) Prion induction involves an ancient system for the sequestration of aggregated proteins and heritable changes in prion fragmentation. *Proc Natl Acad Sci USA* 107:8633–8638.
3. Tyedmers J, Madariaga ML, Lindquist S (2008) Prion switching in response to environmental stress. *PLoS Biol* 6:e294.
4. Rizzo MA, Springer GH, Granada B, Piston DW (2004) An improved cyan fluorescent protein variant useful for FRET. *Nat Biotechnol* 22:445–449.
5. Wach A, Brachat A, Alberti-Segui C, Rebischung C, Philippsen P (1997) Heterologous HIS3 marker and GFP reporter modules for PCR-targeting in Saccharomyces cerevisiae. *Yeast* 13:1065–1075.
6. Zhou P, Derkatch IL, Liebman SW (2001) The relationship between visible intracellular aggregates that appear after overexpression of Sup35 and the yeast prion-like elements [PSI(+)] and [PIN(+)]. *Mol Microbiol* 39:37–46.
7. Bagriantsev SN, Gracheva EO, Richmond JE, Liebman SW (2008) Variant-specific [PSI+] infection is transmitted by Sup35 polymers within [PSI+] aggregates with heterogeneous protein composition. *Mol Biol Cell* 19:2433–2443.
8. Winkler J, Tyedmers J, Bukau B, Mogk A (2012) Hsp70 targets Hsp100 chaperones to substrates for protein disaggregation and prion fragmentation. *J Cell Biol* 198: 387–404.
9. Becker J, Walter W, Yan W, Craig EA (1996) Functional interaction of cytosolic hsp70 and a DnaJ-related protein, Ydj1p, in protein translocation in vivo. *Mol Cell Biol* 16: 4378–4386.
10. Hawes P, Netherton CL, Mueller M, Wileman T, Monaghan P (2007) Rapid freeze-substitution preserves membranes in high-pressure frozen tissue culture cells. *J Microsc* 226:182–189.
11. Zheng SQ, et al. (2007) UCSF tomography: An integrated software suite for real-time electron microscopic tomographic data collection, alignment, and reconstruction. *J Struct Biol* 157:138–147.
12. Mastronarde DN (1997) Dual-axis tomography: An approach with alignment methods that preserve resolution. *J Struct Biol* 120:343–352.
13. Castaño-Díez D, Scheffer M, Al-Amoudi A, Frangakis AS (2010) Alignator: A GPU powered software package for robust fiducial-less alignment of cryo tilt-series. *J Struct Biol* 170:117–126.
14. Förster F, Pruggnaller S, Seybert A, Frangakis AS (2008) Classification of cryo-electron sub-tomograms using constrained correlation. *J Struct Biol* 161:276–286.

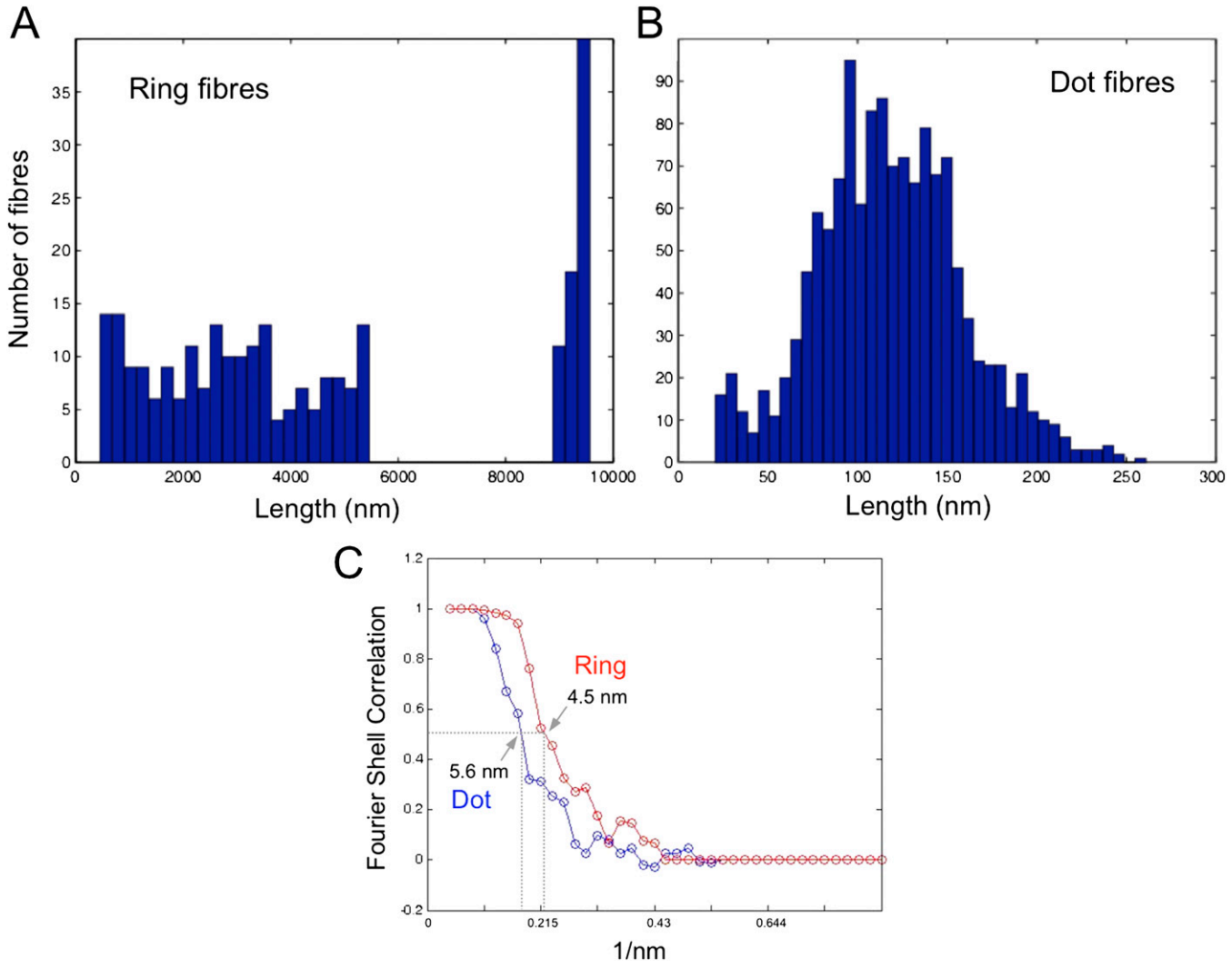

Fig. S1. Graph of fiber lengths in ring (*A*) and dot (*B*) aggregates. Most ring fibers are ~10 μm long, whereas the length distribution of dot fibers peaks at ~110 nm. Estimates for the resolution of the 3D maps obtained by subtomogram averaging were obtained by Fourier shell correlation, in which the data set is divided into two halves, and the two resulting maps are compared. The resolution value is estimated from the point at which the correlation between the two maps has dropped to 50% of the maximum. The Fourier shell correlation curves in *C* give a resolution of 4.5 nm for the ring average and 5.6 nm for the dot average.

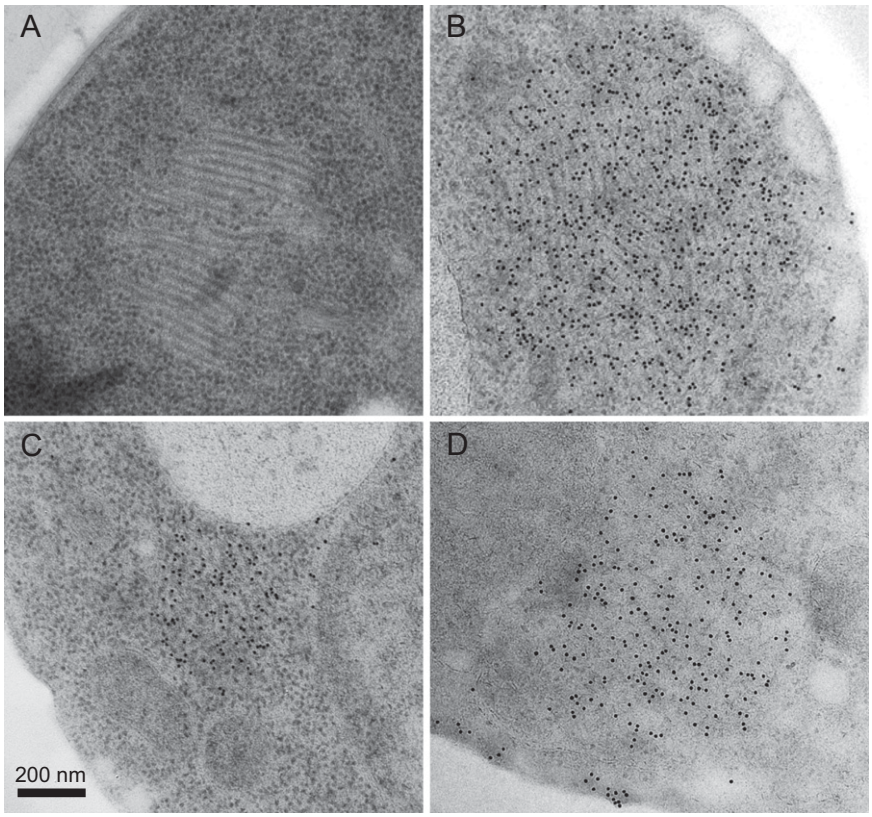

Fig. S2. (*A*) Freeze-substituted section image of a dot formed from NM without the GFP tag and tagged with HA. The fiber array appears very similar to those observed with NM-GFP. (*B–D*) Freeze-substituted sections of dot aggregates composed of NM-YFP labeled with gold–anti-YFP, in cells with Ssa2, -3, and -4 deleted (Ssa2–4Δ) after 1.5 h of incubation at 37° (*B*), with a temperature-sensitive (ts) Ssa1 and Ssa2–4Δ after incubation at 25 °C (*C*) and with ts Ssa1 and Ssa2–4Δ after 1.5 h of incubation at 37 °C (*D*). The ts Ssa1 is functional at 25 °C but not at 37 °C. The cells with Ssa2–4 deleted showed a range of dot features, with some less well ordered and smaller than the one shown in *B*. The fiber packing appeared looser and more disordered in the Ssa1 ts, Ssa2–4Δ cells at 37 °C.

Movie S1. Paths of individually segmented fibers in a dot reconstructed from tomograms of seven serial sections. The fibers are organized in a mosaic of bundles with relatively uniform length and spacing.

Movie S1